Molecular & Cellular Biomechanics
DOI:10.32604/mcb.2020.08750
Article

Tech Science Press

A Patient-Specific Computational Fluid Dynamic Model of Middle Cerebral Artery Aneurysm Before and One Year After Surgery

Shicheng He[1], Juhui Qiu[1], Wanling Liu[1], Tieying Yin[1], Dechuan Zhang[2,*], Donghua Liao[3,4], Haijun Zhang[5], Yuxia Yin[5] and Guixue Wang[1,*]

[1]Key Laboratory for Biorheological Science and Technology of Ministry of Education, State and Local Joint Engineering Laboratory for Vascular Implants, Bioengineering College of Chongqing University, Chongqing, 400030, China
[2]Chongqing Hospital of Traditional Chinese Medicine, Chongqing, 400021, China
[3]GIOME Academia, Department of Clinical Medicine, Aarhus University, Aarhus, Denmark
[4]Mech-Sense, Department of Gastroenterology, Aalborg University Hospital, Aalborg, Denmark
[5]National United Engineering Laboratory for Biomedical Material Modification, Dezhou, 251100, China
*Corresponding Authors: Dechuan Zhang. Email: cqggzdc@163.com; Guixue Wang. Email: wanggx@cqu.edu.cn
Received: 04 October 2019; Accepted: 23 December 2019

Abstract: Computational fluid dynamics (CFD) has been widely used for studying intracranial aneurysm hemodynamics, while its use for guiding clinical strategy is still in development. In this study, CFD simulations helped inform treatment decision for a middle cerebral artery (MCA) aneurysm case was investigated. A patient with a 10.4 × 9.8 mm aneurysm attached with a small aneurysm at the edge of the trifurcation in the left MCA was included in this study. For removing the MCA aneurysm, two scenarios were considered: Plan-A involved clipping the small aneurysm and Plan-B involved clipping the whole aneurysm. A suitable treatment plan was decided by comparing the clinical measurements and CFD analysis between these two plans. One-year after the surgery, the CFD analysis was conducted again on the post-operative aneurysm model to verify the selected surgical plan in terms of morphometric and hemodynamic properties changes in the aneurysm. Based on the CFD simulation and clinical experience, surgical Plan-A was adopted. One-year after the surgery, both the hemodynamic and morphological properties improved in the post-operative aneurysm model, indicating the recovery of the patient. The patient-specific aneurysm CFD analysis can help to determine a better surgical plan for patients with special cerebral aneurysms. This study showed how CFD analysis can be used to aid clinical diagnosis and treatment.

Keywords: Cerebral aneurysms; computational fluid dynamics; computed tomography angiography; hemodynamics

Abbreviations
CFD: computational fluid dynamics
CTA: computed tomography angiography
MCA: middle cerebral artery

OSI: oscillatory shear index
TAWSS: time averaged wall shear stress
WSS: wall shear stress

1 Introduction

Intracranial aneurysm is a kind of destructive cerebrovascular disease, which is characterized by the pathological enlargement of local cerebral arteries. Sudden rupture of middle cerebral aneurysms can cause subarachnoid hemorrhage, associating with serious morbidity and mortality [1]. Size and location have been identified as important aneurysm-specific predictors of rupture in both single and multiple aneurysms [2,3]. While the rupture incidence of small aneurysms and multiple aneurysms makes the point of view controversial [4]. Therefore, more and more researches focused on better predictors for aneurysm rupture [5]. Among all the risk factors involved, the hemodynamics of the aneurysm are thought to be the most fundamental one. Previous studies have shown the hemodynamic parameters, including wall shear stress (WSS), oscillatory shear index (OSI) and flow patterns play significant role in the rupture of an aneurysm, despite that debate whether low or high WSS that really makes difference in the aneurysm formation or rupture still existence [6-9]. With the advancement of angiography technology, researches based on patient-specific aneurysm model have been greatly promoted since three-dimensional image provides detailed anatomical features that are often neglected in idealized aneurysm geometries [10,11]. Clinically, the treatment strategies of aneurysms mainly include clipping and endovascular interventional embolization. The choice depends on the size of the aneurysm, rupture status, whether the patient's physical condition can withstand the trauma of craniotomy [12,13].

Most of the existed studies were case-based theoretical analysis and mainly focused on describing the causes of the aneurysm formation or rupture, only few of them have used the computational fluid dynamics (CFD) simulation to determine diagnosis and treatment [14-20]. For this reason, a case of patient with aneurysms on the middle cerebral artery (MCA) was included in the present study. Two virtual surgical plans were considered from the Computed tomography angiography (CTA) scanning. The CFD simulations of the pre-operative model and the models of the two considered surgical plans were analyzed. A better operation decision was made from comprehensive perspectives of the clinical experiences and the hemodynamic of the artery. One-year after the surgery, the patient's CTA data was obtained again for further numerical simulations to verify the choice of operation selection. Thus, the objective of this study was to explore the feasibility of CFD in the treatment of aneurysms, and shed some lights on the clinical application of CFD method.

2 Materials and Methods

2.1 Patient

The patient (A 52-year-old female diagnosed with a special MCA aneurysm) was admitted to the hospital for a sudden consciousness disorder in 2017. Primary intracranial CTA data showed there were an unruptured aneurysm of the left MCA in size 10.4 × 9.8 mm attached with a small aneurysm at the edge in the trifurcation and an unruptured aneurysm of the right MCA in size 8 × 5.9 mm in the bifurcation (Figs. 1a1 and 1a2). Considering rupture of the left aneurysm would occur at any time due to the abnormal size and morphology, it was required to consider clipping the left aneurysm as soon as possible and we examined different clipping positions. The patient then underwent intracranial CTA and internal carotid artery ultrasound (Fig. 1d). The CFD model of the aneurysm in the left MCA was built from the CTA images, and the ultrasound data was used for extracting inlet velocity waveform by MATLAB programming. The pre-operative model and models with two considered clipping positions were predicted and simulated by using the CFD analysis. In 2018, the patient visited the

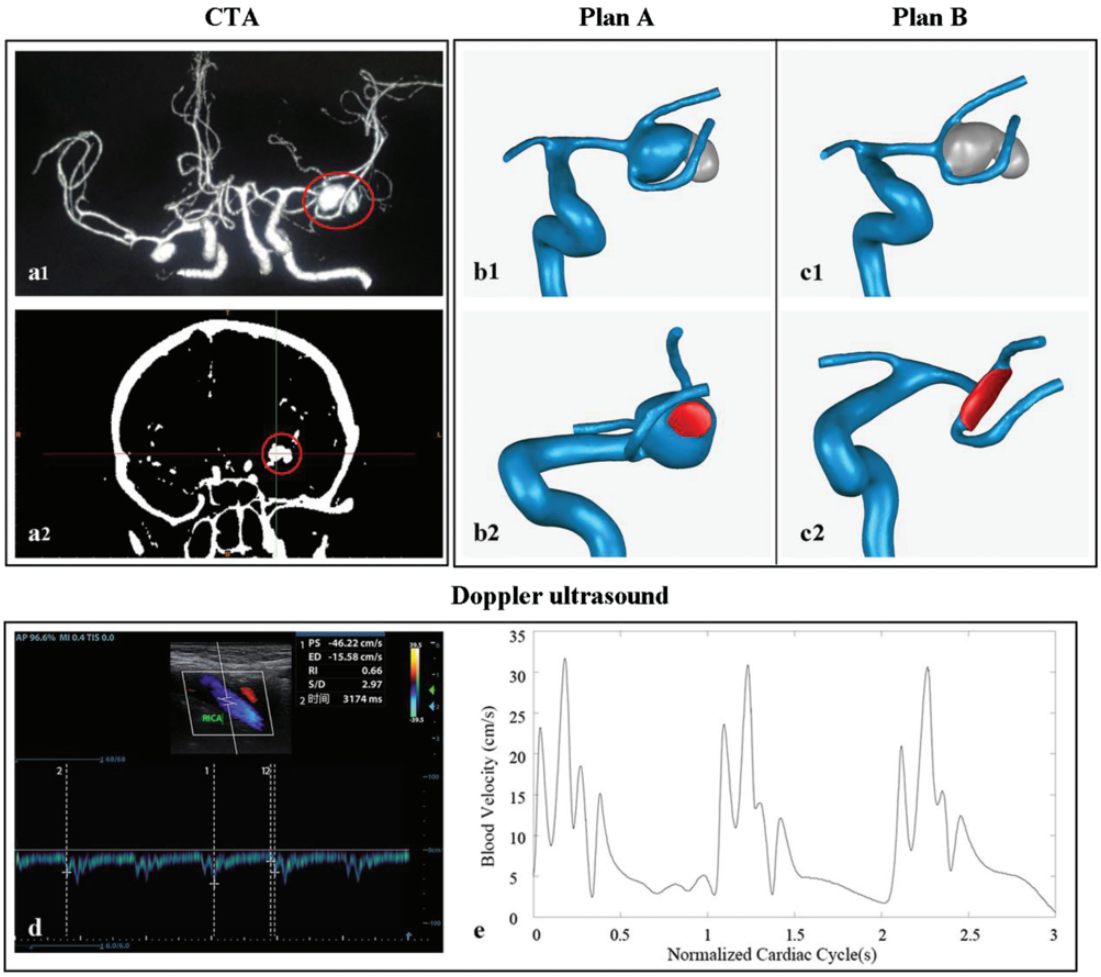

Figure 1: Images of an MCA aneurysm from intracranial CTA at time of admission and reconstructed 3D geometric model. Red circle points to the left aneurysm. (a) Primary intracranial CTA imaging. (b) Plan-A, clipping the small aneurysm, and the wounded area (red area indicates the clipping area of the aneurysm during virtual operation procedure) is around 20 mm^2. (c) Plan-B, clipping the whole aneurysm and the clipping area is around 50 mm^2. (d) Internal carotid artery ultrasound recording. (e) Profile of inlet flow waveforms during the cardiac cycle

hospital for a reexamination. CTA images measurement was acquired again, the imaging data showed the remained aneurysm flattened and decreased significantly to size 4.6 × 7.2 mm. The CFD model for the post-operative aneurysm was thereafter built based on the CTA imaging. The model analysis showed the hemodynamic and morphological properties in the aneurysm improved significantly comparing with those before the operation. Written informed consent was obtained from this patient, and the research was permitted by the ethics committee of Chongqing Hospital of Traditional Chinese Medicine.

2.2 3D Models and Surgical Plans

The medical images were obtained from Chongqing Hospital of Traditional Chinese Medicine. The pre- and post- operative CTA images in Digital Imaging in Communications in Medicine (DICOM) format were imported into the software Mimics 15.0 (Materialise, Leuven, Belgium) to reconstruct the 3D artery model from internal carotid artery to MCA segment. We imported the obtained 3D artery

model into the software Geomagic Studio 12.0 (Geomagic, North Carolina, USA) to build the pre-operative artery model, models in two different clipping plans, and the post-operative model. The models with two clipping plans are: the artery model clipping the lateral aneurysm for Plan-A (Fig. 1b), the model clipping the whole aneurysm for Plan-B (Fig. 1c). The post-operative artery model was built from CTA images taken one year after the operation.

2.3 Computational Fluid Dynamic (CFD) Model

The CFD analysis was done by using ICEM CFD v.15 and ANSYS CFX v.15 (ANSYS, Canonsburg, PA, USA). During the CFD analysis, blood was assumed to be homogeneous and incompressible Newtonian fluid with viscosity and density of 0.0035 Pa·s and 1060 kg/m^3. The arterial wall was assumed to be rigid with a non-slip boundary and all inlets were cut at the same locations near the fourth cervical vertebra [21-23]. A pulsatile period velocity profile recorded through internal carotid Doppler ultrasound was used as the inlets boundary condition (Figs. 1d and 1e). Zero-pressure boundary conditions were set at all outlets. Three cardiac cycle simulations were performed for numerical stability and the calculation achieved convergence in the second cardiac cycle. Same boundary conditions were adopted in all simulations, and results of peak systolic from the third cardiac cycle were collected as outputs for the final analysis (Fig. 1e). All the CFD analyses were accomplished on a high-performance computer (DELL PRECISION TOWER 7910 2.4 GHz workstations) having 2 × 12 core processors and 64 GB of RAM.

2.4 Data Analysis

2.4.1 Hemodynamic Parameters

Hemodynamic parameters, including wall shear stress (WSS), velocity, pressure, time averaged wall shear stress (TAWSS) and oscillatory index (OSI), were used to evaluate the hemodynamic properties of the aneurysm. All parameters were obtained by post-processing of the CFD analysis. Definitions of these parameters are showed in Appendices.

2.4.2 Morphologic Parameters

Morphological parameters included: neck width (averaged aneurysm neck diameter), maximum height (the maximum distance from neck plane to the aneurysm dome), volume and aspect ratio (the ratio between the maximal height and the neck width) of the aneurysm. The parameters were measured from the pre-operative model, Plan-A model and the post-operative model.

3 Results

3.1 Pre-operative and Plan- A & B Models

Figure 2 shows the WSS and 3D streamline distributions of the aneurysm dome in the pre-operative model and plan- A and B models. In the pre-operative model, the WSS in the neck position of the small aneurysm was higher than the rest of the aneurysm (Mean ± SD: 27.65 ± 13.67 Pa *vs*. 5.27 ± 3.63 Pa, Fig. 2a1). Moreover, the vortices and blood stagnation area in the small aneurysm were more obvious than the other parts of the aneurysm (Fig. 2a2). In Plan-A model, comparing with the pre-operative model, the hemodynamic environment in the remained aneurysm improved, and represented by moving the high WSS area to the lateral wall of the remained aneurysm, increasing the blood flow velocity, and decreasing the vortices numbers (Fig. 2b). In Plan-B model, the hemodynamic characteristics changed significantly by removing the whole aneurysm, however, a significant low shear flow appeared at the trifurcation of the blood vessels, which might lead to blood stagnation and regeneration of aneurysm later (Fig. 2c).

The overall pressure distributions for all three models showed a similar pattern from inlet to outlet of the flow (Figs. 2d-2f). In the pre-operative model, there was a significant high-pressure area up to 3.4 kPa at the neck area of the small aneurysm (Fig. 2g). In Plan-A model, the high-pressure area enlarged and distributed

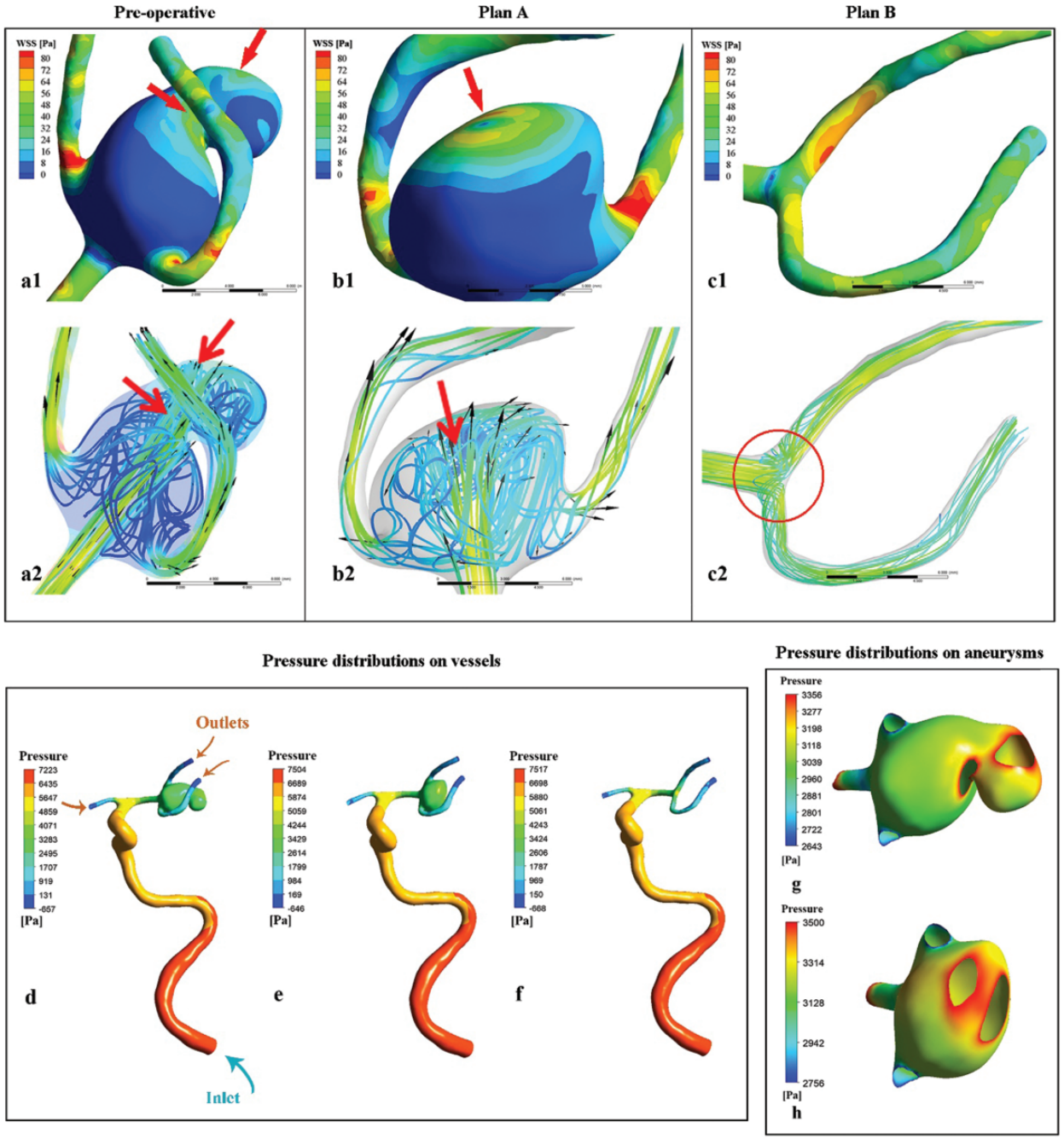

Figure 2: WSS (a1, b1, c1), pressure (d, e, f) distributions at peak systole on the vessels and streamlines (a2, b2, c2) inside the vessel in three different virtual models. Red arrows indicate the higher WSS area, and the red circle indicates the vessel trifurcation. (a1, a2 & d) Pre-operative aneurysm model. (b1, b2 & e) Plan- A model. (c1, c2 & f) Plan- B model. (g & h) pressure distributions on the aneurysm dome in pre-operative model and Plan-A model

more evenly than that in the pre-operative model (Fig. 2h). Fig. 3 shows the TAWSS and OSI distributions in all three models, for the pre-operative model, the TAWSS was higher at the neck of the small aneurysm and the OSI was higher around the neck of the main aneurysm and the lateral wall of the small aneurysm

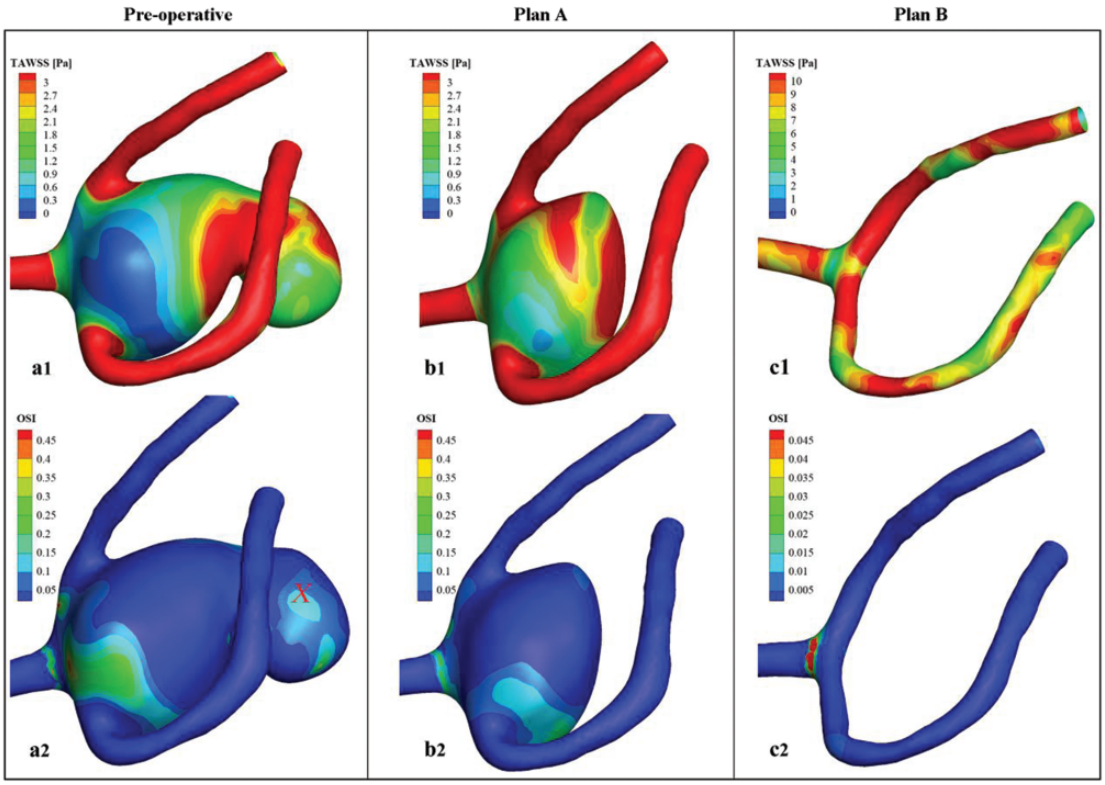

Figure 3: TAWSS (a1, b1, c1) and OSI (a2, b2, c2) distributions on the aneurysm dome in three virtual models. (a1 & a2) Pre-operative aneurysm model. X in a2 marks a possible high risky rupture location of the aneurysm. (b1 & b2) Plan-A model. (c1 & c2) Plan-B model

(Fig. 3a). In Plan-A model, OSI distributed similarly to that of the pre-operative model and the TAWSS was higher on the lateral wall of the remained aneurysm (Fig. 3b). Comparing to the pre-operative- and Plan-A models, the TAWSS was the highest, while the OSI was the lowest in Plan-B model (Mean ± SD for TAWSS: 9.92 ± 3.30 Pa in Plan B model *vs*. 1.55 ± 1.43 Pa in pre-operative model and 1.87 ± 1.38 Pa in Plan A model; Mean ± SD for OSI: 0.017 ± 0.03 in Plan B model *vs*. 0.198 ± 0.12 in pre-operative model and 0.077 ± 0.07 in Plan A model, Fig. 3c). Figs. 2 and 3 showed improvements of the hemodynamic characteristics in Plan-A model, especially for the blood flow and TAWSS distribution at the aneurysm dome. Although the hemodynamic properties also improved in Plan-B model, the significant low shear flow in the trifurcation and a bigger surgical wound areas (the red areas in Figs. 1b and 1c) in Plan-B model could likely lead to a regeneration of the aneurysm in the future. By taking the hemodynamic improvements as well as the surgery procedure into account, we selected the more conservative treatment Plan-A for the patient.

3.2 Post-Operative Model

Comparing to Plan-A model, the post-operative model had: 1) a lower aneurysm pressure (Maximum pressure: 1.685 kPa in the post-operative model *vs.* 3.592 kPa in Plan A model); 2) less number of the vortices; and 3) more evenly WSS distribution (the peak systolic WSS in aneurysm dome range: (0.103 Pa, 15.16 Pa) in the post-operative model *vs.* (0.109 Pa, 65.93 Pa) in Plan A model) (Fig. 4). These indicated the hemodynamic improvement of the post-operative model.

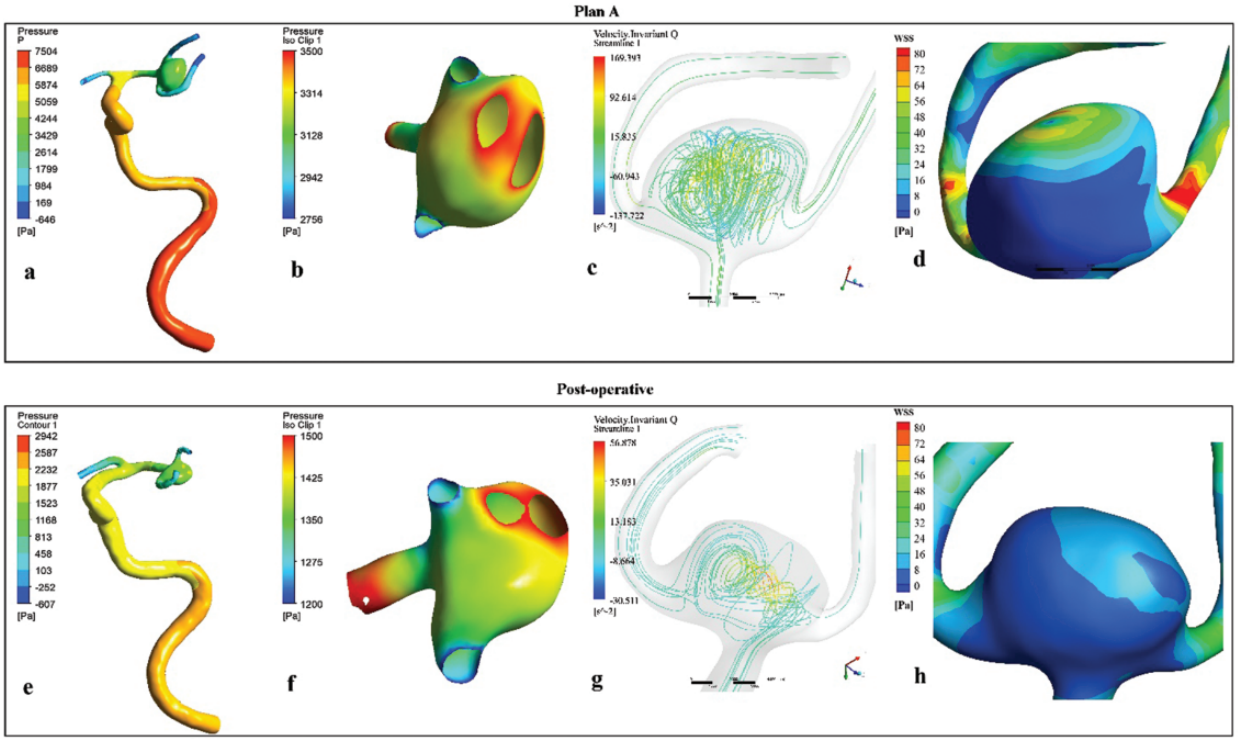

Figure 4: Comparison of the simulation results between the Plan-A model (a, b, c, d) and the one year post-operative model (e, f, g, h). a, b and e, f showed the pressure on the aneurysm surface decreased significantly at the post-operative model. c & g showed the vortices number decreased in the aneurysm in the post-operative model. d & h showed the shear stress distribution was more uniform and the gradient was lower in the one-year postoperative model

3.3 Morphological Change of the Aneurysm

Table 1 shows the aneurysm morphological change from the pre-operative state to the post-operative state. The original aneurysm volume was around 492 mm^3, by clipping the small aneurysm, all morphological parameters in Plan-A model decreased significantly than that in the pre-operative state. One year after the operation, the aneurysm volume decreased to about 50% of Plan-A model, and about 25% of the pre-operative model; the aspect ratio decreased to about 76% and 42% of Plan-A and the pre-operative model.

Table 1: Morphological parameters of the aneurysm

Artery model	Neck width (mm)	Maximal height (mm)	Volume (mm^3)	Aspect ratio
Pre-operative	8.918	12.094	496	1.356
Plan A	8.918	6.764	282	0.758
Post-operative	7.472	4.309	122	0.577

Note: Neck width: averaged aneurysm neck diameter; Maximal height: the maximum distance from neck plane to the aneurysm dome; Aspect ratio: the ration between the maximal height and the neck width. The hemodynamic and the morphological improvements after the operation indicating a good recovery of the patient by means of the surgical Plan-A, and the treatment Plan-A had a good benefit to the patient.

4 Discussion

Clinical diagnosis of intracranial aneurysms is usually based on morphological features and clinical experience of the clinicians, the hemodynamic factors which can be used to aid clinical diagnosis and treatment are mostly ignored. In this study, the hemodynamic characteristics of a rare unruptured MCA aneurysm was simulated on a patient-specific model at the admission time and one-year post-operation. A suitable surgical plan was selected from comprehensive perspectives by comparing the simulated hemodynamic properties between the pre-operative model and the virtual models in two different clipping plans. One-year after the operation, both the hemodynamic and the morphological properties improved significantly, indicating the good effectiveness of the selected treatment Plan.

In recent years, the hemodynamic characteristics of aneurysms and their arteries are widely used as factors to estimate the initiation, growth and rupture of the intracranial aneurysms [6,18,24-28]. Many studies have showed the high WSS drives intracranial aneurysms formation and rupture [29-31], whereas several computational studies have pointed the low WSS correlated to the aneurysm rupture [32-34]. Meng et al. [35] and Zhang et al. [29] found that the high WSS combined with a positive WSS gradient triggered a mural-cell-mediated pathway, which could associate with the growth and rupture of the intracranial aneurysm. Moreover, the increased pressure over the aneurysm surface may trigger the growth or rupture because, as an aneurysm is stretched, weak blood vessel walls are vulnerable to the large pressure gradient [36-38]. From hemodynamic points of view, the unruptured aneurysms can be characterized as a simple and stable flow field, large impact area and wide inject inflow, while the ruptured aneurysms with unstable flow field, small impact area and narrow inject inflow [38]. The study from Cebral et al. showed the cerebral aneurysms with small impingement sizes were 6.3 times more likely to have experienced rupture compared with aneurysms with relatively large impingement zones [39]. In WSS and streamline distributions of our models (Figs. 2a2 and 2b2), both pre-operative and Plan-A models had a concentrated impingement inject flow area in the aneurysm, and with high WSS in the area. However, the impingement jet area was wider in the Plan-A model, indicting the remained aneurysm are more stable and consequently with a low rapture rate after the Plan-A surgery. Sejkorová et al. [19] found that OSI at the rupture location increased and was higher than that on the dome before a rupture. The CFD analysis in our pre-operative model showed there were a high OSI and high WSS area in the attached aneurysm, means a high rupture risk of the area (Fig. 2a). Therefore, the small aneurysm must be clipped as soon as possible for reducing the high rupture risk of the aneurysm. By comparing the hemodynamic properties between Plan-A and Plan-B models, the Plan-B model showed an obvious turbulence in the trifurcation of the blood vessels. The hemodynamic abnormalities that associates with the endothelial dysfunction and thus can likely lead to the aneurysm regeneration later [40-42].

The other generally recognized cause of aneurysm rupture is the morphological characteristics of the aneurysm including various shape, aneurysm size, AR [43]. Backes et al. [44] reported that AR and irregular shape were associated with aneurysm rupture in 124 patients with 302 multiple aneurysms, the results found that AR > 1.3 and irregular shape are associated with aneurysm rupture independent of aneurysm size and location. Lu et al. [2] identified size >5 mm as a risk factor for aneurysm rupture in a cohort of 294 patients with multiple aneurysms. In our present research, we have measured the morphological parameters of aneurysms in pre-operative, plan-A and post-operative model (Tab. 1). For pre-operative model, AR is over 13 and indicates the instability of the aneurysm. While by clipping the daughter aneurysm, AR significantly decreased to around 0.7 with a shrink size and volume. One year after surgery, AR reduced to a lower level and the volume of aneurysm is one fourth of that before operation, indicating that the patient recovered well through the Plan A treatment. Therefore, on the basis of the CFD simulations, morphological properties of the aneurysm [7,37,40] and clinical experiences, from a comprehensive perspective the treatment Plan-A was selected for the patient.

Although the data from our study appear to suggest that hemodynamic characteristics determined by CFD analysis can be used to aid the clinical diagnosis and treatment plan decision, these data must be considered preliminary. This study relied on an assumption that the artery is rigid with no deformation during the blood flow, however, the artery as well as the aneurysm may undergo a variety of structural changes during the pulsatile flow. That could be overcome later by using the fluid-structure interaction model analysis. The study limited by using only one specific case, the large population model with large variety of the aneurysms should be taken into account in our future investigations. Another limitation in this study is the in vivo hemodynamic environment of the patient changed from pre- to post- operation, thus the boundary conditions obtained from the internal carotid Doppler ultrasound measurement differed between the pre- and post-operative models. That was a main cause of the significantly lower pressure and WSS in the post-operative model. However, the lower pressure and WSS values in the post-operation state also implied a good recovery of the patient.

5 Conclusion

This study designed two virtual aneurysm clipping surgical plans for a patient with a 10.4 × 9.8mm aneurysm attached with a small aneurysm at the edge of the trifurcation in the left MCA. Numerical CFD simulations were conducted in the pre-operative model and the models with the two treatment plans for aiding a determination of the best surgical option. The one-year follow-up CFD simulation results showed an improved hemodynamic and morphometric characters of the aneurysm in the patient, indicating the CFD analysis might can be used on aiding clinical diagnosis and treatment of the intracranial aneurysm.

Acknowledgement: This study was supported by grants from the National Natural Science Foundation of China [grant number 31971242, 31701275]; Chongqing Science and Technology Bureau (cstc2019jcyj-zdxm0033), the Fundamental Research Funds for the Central Universities [grant number 2019CDYGZD008, 2019CDXYSG0004]; the Chongqing Engineering Laboratory in Vascular Implants and the Public Experiment Center of State Bioindustrial Base (Chongqing); and the Karen Elise Jensens Foundation (grant number 903959, Denmark).

Conflict of Interests: The authors declare that they have no conflicts of interest to report regarding the present study.

Author Contributions: Conception and design: S. He, D. Zhang, G. Wang. Acquisition of data: D. Zhang, W. Liu, J. Qiu. Drafting the article: S. He, W. Liu, D. Liao. Statistical analysis, interpretation and discussion: S. He, T. Yin, H. Zhang, D. Liao. Critical revision of the of manuscript: D. Liao, G. Wang, H. Zhang. Approved the final version of the manuscript on behalf of all authors: G. Wang. Study supervision: G. Wang.

References

1. Jansen, I. G. H., Schneiders, J. J., Potters, W. V., van Ooij, P., van den Berg, R. et al. (2014). Generalized versus patient-specific inflow boundary conditions in computational fluid dynamics simulations of cerebral aneurysmal hemodynamics. *American Journal of Neuroradiology, 35(8),* 1543–1548. DOI 10.3174/ajnr.A3901.
2. Lu, H., Tan, H., Gu, B., Wu, W., Li, M. (2013). Risk factors for multiple intracranial aneurysms rupture: a retrospective study. *Clinical Neurology and Neurosurgery, 115(6),* 690–694. DOI 10.1016/j.clineuro.2012.08.011.
3. Xu, J., Yu, Y., Wu, X., Wu, Y., Jiang, C. et al. (2013). Morphological and hemodynamic analysis of mirror posterior communicating artery aneurysms. *PLoS One, 8(1), e55413*. DOI 10.1371/journal.pone.0055413.
4. Doddasomayajula, R., Chung, B. J., Mut, F., Jimenez, C. M., Hamzei-Sichani, F. et al. (2017). Hemodynamic characteristics of ruptured and unruptured multiple aneurysms at mirror and ipsilateral locations. *American Journal of Neuroradiology, 38(12),* 2301–2307. DOI 10.3174/ajnr.A5397.

5. Detmer, F. J., Chung, B. J., Jimenez, C., Hamzei-Sichani, F., Kallmes, D. et al. (2019). Associations of hemodynamics, morphology, and patient characteristics with aneurysm rupture stratified by aneurysm location. *Neuroradiology, 61(3),* 275–284. DOI 10.1007/s00234-018-2135-9.
6. Raghavan, M. L., Ma, B., Harbargh, R. E. (2005). Quantified aneurysm shape and rupture risk. *Journal of Neurosurgery, 102(2),* 355–362. DOI 10.3171/jns.2005.102.2.0355.
7. Longo, M., Granata, F., Racchiusa, S., Mormina, E., Grasso, G. et al. (2017). Role of hemodynamic forces in unruptured intracranial aneurysms: an overview of a complex scenario. *World Neurosurgery, 105,* 632–642. DOI 10.1016/j.wneu.2017.06.035.
8. Jou, L. D., Lee, D. H., Morsi, H., Mawad, M. E. (2008). Wall shear stress on ruptured and unruptured intracranial aneurysms at the internal carotid artery. *American Journal of Neuroradiology, 29(9),* 1761–1767. DOI 10.3174/ajnr.A1180.
9. Sun, Q., Groth, A., Aach, T. (2012). Comprehensive validation of computational fluid dynamics simulations of in-vivo blood flow in patient-specific cerebral aneurysms. *Medical Physics, 39(2),* 742–754. DOI 10.1118/1.3675402.
10. Jing, L., Fan, J., Wang, Y., Li, H., Wang, S. et al. (2015). Morphologic and hemodynamic analysis in the patients with multiple intracranial aneurysms: ruptured versus unruptured. *PLoS One, 10(7), e0132494*. DOI 10.1371/journal.pone.0132494.
11. Omodaka, S., Sugiyama, S., Inoue, T., Funamoto, K., Fujimura, M. et al. (2012). Local hemodynamics at the rupture point of cerebral aneurysms determined by computational fluid dynamics analysis. *Cerebrovascular Diseases, 34(2),* 121–129. DOI 10.1159/000339678.
12. Janiga, G., Daróczy, L., Berg, P., Thévenin, D., Skalej, M. et al. (2015). An automatic CFD-based flow diverter optimization principle for patient-specific intracranial aneurysms. *Journal of Biomechanics, 48(14),* 3846–3852. DOI 10.1016/j.jbiomech.2015.09.039.
13. Saqr, K. M., Rashad, S., Tupin, S., Niizuma, K., Hassan, T. et al. (2019). What does computational fluid dynamics tell us about intracranial aneurysms? A meta-analysis and critical review. *Journal of Cerebral Blood Flow & Metabolism,* 1–19. DOI 10.1177/0271678x19854640.
14. Wan, H., Ge, L., Huang, L., Jiang, Y., Leng, X. et al. (2019). Sidewall aneurysm geometry as a predictor of rupture risk due to associated abnormal hemodynamics. *Frontiers in Neurology, 10,* 841. DOI 10.3389/fneur.2019.00841.
15. Xiang, J., Natarajan, S. K., Tremmel, M., Ma, D., Mocco, J. et al. (2011). Hemodynamic–morphologic discriminants for intracranial aneurysm rupture. *Stroke, 42(1),* 144–152. DOI 10.1161/STROKEAHA.110.592923.
16. Zhang, Y., Mu, S., Chen, J., Wang, S., Li, H. et al. (2011). Hemodynamic analysis of intracranial aneurysms with daughter blebs. *European Neurology, 66(6),* 359–367. DOI 10.1159/000332814.
17. Skodvin, T.Ø., Evju, Ø., Helland, C. A., Isaksen, J. G. (2018). Rupture prediction of intracranial aneurysms: a nationwide matched case-control study of hemodynamics at the time of diagnosis. *Journal of Neurosurgery, 129(4),* 854–860. DOI 10.3171/2017.5.JNS17195.
18. Lv, N., Wang, C., Karmonik, C., Fang, Y., Xu, J. et al. (2016). Morphological and hemodynamic discriminators for rupture status in posterior communicating artery aneurysms. *PLoS One, 11(2), e0149906*. DOI 10.1371/journal.pone.0149906.
19. Sejkorova, A., Dennis, K. D., Svihlova, H., Petr, O., Lanzino, G. et al. (2017). Hemodynamic changes in a middle cerebral artery aneurysm at follow-up times before and after its rupture: a case report and a review of the literature. *Neurosurgical Review, 40(2),* 329–338. DOI 10.1007/s10143-016-0795-7.
20. Brunozzi, D., Theiss, P., Andrews, A., Amin-Hanjani, S., Charbel, F. T. et al. (2019). Correlation between laminar wall shear stress and growth of unruptured cerebral aneurysms: an in vivo assessment. *World Neurosurgery, 131,* e599–e605. DOI 10.1016/j.wneu.2019.08.005.
21. Alastruey, J., Xiao, N., Fok, H., Schaeffter, T., Figueroa, C. A. (2016). On the impact of modelling assumptions in multi-scale, subject-specific models of aortic haemodynamics. *Journal of the Royal Society Interface, 13(119),* 20160073. DOI 10.1098/rsif.2016.0073.
22. Chiastra, C., Morlacchi, S., Gallo, D., Morbiducci, U., Cárdenes, R. et al. (2013). Computational fluid dynamic simulations of image-based stented coronary bifurcation models. *Journal of the Royal Society Interface, 10(84),* 20130193. DOI 10.1098/rsif.2013.0193.

23. Berg, P., Saalfeld, S., Voss, S., Beuing, O., Janiga, G. (2019). A review on the reliability of hemodynamic modeling in intracranial aneurysms: why computational fluid dynamics alone cannot solve the equation. *Neurosurgical Focus, 47(1),* E15. DOI 10.3171/2019.4.FOCUS19181.
24. TISoUIA, I. (1998). Unruptured intracranial aneurysms—risk of rupture and risks of surgical intervention. *New England Journal of Medicine, 339(24),* 1725–1733. DOI 10.1056/NEJM199812103392401.
25. Morita, A., Kirino, T., Hashi, K., Aoki, N., Fukuhara, S. et al. (2012). The natural course of unruptured cerebral aneurysms in a Japanese cohort. *New England Journal of Medicine, 366(26),* 2474–2482. DOI 10.1056/NEJMoa1113260.
26. Valen-Sendstad, K., Steinman, D. A. (2014). Mind the gap: impact of computational fluid dynamics solution strategy on prediction of intracranial aneurysm hemodynamics and rupture status indicators. *American Journal of Neuroradiology, 35(3),* 536–543. DOI 10.3174/ajnr.A3793.
27. Matsukawa, H., Kamiyama, H., Kinoshita, Y., Saito, N., Hatano, Y. et al. (2018). Morphological parameters as factors of 12-month neurological worsening in surgical treatment of patients with unruptured saccular intracranial aneurysms: importance of size ratio. *Journal of Neurosurgery, 131(3),* 852–858. DOI 10.3171/2018.4.JNS173221.
28. Qin, H., Yang, Q., Zhuang, Q., Long, J., Yang, F. et al. (2017). Morphological and hemodynamic parameters for middle cerebral artery bifurcation aneurysm rupture risk assessment. *Journal of Korean Neurosurgical Society, 60(5),* 504–510. DOI 10.3340/jkns.2017.0101.009.
29. Zhang, X., Karuna, T., Yao, Z., Duan, C., Wang, X. et al. (2018). High wall shear stress beyond a certain range in the parent artery could predict the risk of anterior communicating artery aneurysm rupture at follow-up. *Journal of Neurosurgery, 131(3),* 868–875. DOI 10.3171/2018.4.JNS173179.
30. Cebral, J. R., Mut, F., Weir, J., Putman, C. (2011). Quantitative characterization of the hemodynamic environment in ruptured and unruptured brain aneurysms. *American Journal of Neuroradiology, 32(1),* 145–151. DOI 10.3174/ajnr.A2419.
31. Cebral, J. R., Sheridan, M., Putman, C. M. (2010). Hemodynamics and bleb formation in intracranial aneurysms. *American Journal of Neuroradiology, 31(2),* 304–310. DOI 10.3174/ajnr.A1819.
32. Zhang, Y., Tian, Z., Jing, L., Zhang, Y., Liu, J. et al. (2016). Bifurcation type and larger low shear area are associated with rupture status of very small intracranial aneurysms. *Frontiers in Neurology, 7,* 169. DOI 10.3389/fneur.2016.00169.
33. Fukazawa, K., Ishida, F., Umeda, Y., Miura, Y., Shimosaka, S. et al. (2015). Using computational fluid dynamics analysis to characterize local hemodynamic features of middle cerebral artery aneurysm rupture points. *World Neurosurgery, 83(1),* 80–86. DOI 10.1016/j.wneu.2013.02.012.
34. Cornelissen, B. M., Schneiders, J. J., Potters, W. V., van den Berg, R., Velthuis, B. K. et al. (2015). Hemodynamic differences in intracranial aneurysms before and after rupture. *American Journal of Neuroradiology, 36(10),* 1927–1933. DOI 10.3174/ajnr.A4385.
35. Meng, H., Tutino, V. M., Xiang, J., Siddiqui, A. (2014). High WSS or low WSS? Complex interactions of hemodynamics with intracranial aneurysm initiation, growth, and rupture: toward a unifying hypothesis. *American Journal of Neuroradiology, 35(7),* 1254–1262. DOI 10.3174/ajnr.A3558.
36. Cebral, J. R., Mut, F., Raschi, M., Scrivano, E., Ceratto, R. et al. (2011). Aneurysm rupture following treatment with flow-diverting stents: computational hemodynamics analysis of treatment. *American Journal of Neuroradiology, 32(1),* 27–33. DOI 10.3174/ajnr.A2398.
37. Razaghi, R., Biglari, H., Karimi, A. (2019). Risk of rupture of the cerebral aneurysm in relation to traumatic brain injury using a patient-specific fluid-structure interaction model. *Computer Methods and Programs in Biomedicine, 176,* 9–16. DOI 10.1016/j.cmpb.2019.04.015.
38. Yu, H., Huang, G., Yang, Z., Ludwig, B. R. (2019). Numerical studies of hemodynamic alterations in pre- and post-stenting cerebral aneurysms using a multiscale modeling. *International Journal for Numerical Methods in Biomedical Engineering, 35(11), e3256*. DOI 10.1002/cnm.3256.

39. Cebral, J. R., Castro, M. A., Burgess, J. E., Pergolizzi, R. S., Sheridan, M. J. et al. (2005). Characterization of cerebral aneurysms for assessing risk of rupture by using patient-specific computational hemodynamics models. *American Journal of Neuroradiology, 26(10),* 2550–2559.

40. Bor, A. S., Tiel Groenestege, A. T., terBrugge, K. G., Agid, R., Velthuis, B. K. et al. (2015). Clinical, radiological, and flow-related risk factors for growth of untreated, unruptured intracranial aneurysms. *Stroke, 46(1),* 42–48. DOI 10.1161/STROKEAHA.114.005963.

41. Backes, D., Rinkel, G. J., Laban, K. G., Algra, A., Vergouwen, M. D. (2016). Patient- and aneurysm-specific risk factors for intracranial aneurysm growth: a systematic review and meta-analysis. *Stroke, 47(4),* 951–957. DOI 10.1161/STROKEAHA.115.012162.

42. Lee, U. Y., Jung, J., Kwak, H. S., Lee, D. H., Chung, G. H. et al. (2018). Wall shear stress and flow patterns in unruptured and ruptured anterior communicating artery aneurysms using computational fluid dynamics. *Journal of Korean Neurosurgical Society, 61(6),* 689–699. DOI 10.3340/jkns.2018.0155.

43. Ujiie, H., Tamano, Y., Sasaki, K., Hori, T. (2011). Is the aspect ratio a reliable index for predicting the rupture of a saccular aneurysm? *Neurosurgery, 48(3),* 495–503. DOI 10.1097/00006123-200103000-00007.

44. Backes, D., Vergouwen, M. D., Velthuis, B. K., van der Schaaf, I. C., Bor, A. S. et al. (2014). Difference in aneurysm characteristics between ruptured and unruptured aneurysms in patients with multiple intracranial aneurysms. *Stroke, 45(5),* 1299–1303. DOI 10.1161/STROKEAHA.113.004421.

Appendix

WSS, TAWSS and OSI were defined as:

$$\tau_w = \vec{n} \cdot \vec{\vec{\tau}}_{ij} \tag{1}$$

$$TAWSS = \frac{1}{T}\int_0^T |\tau_w| dt \tag{2}$$

$$\mathrm{OSI} = \frac{1}{2}\left(1 - \frac{\int_0^T \tau_w dt}{\int_0^T |\tau_w| dt}\right) \tag{3}$$

Where τ_w is the wall shear stress (WSS), $\vec{n}$ is the tangential vector to the vessel wall, $\vec{\vec{\tau}}_{ij}$ is the fluid viscous stress tensor and T is the cardiac cycle duration.[18] OSI reflects the changes in the WSS direction and its values range between 0, when there is no oscillatory WSS, and to 0.5 when there is the maximum oscillatory WSS.